

# THE REDSHIFT DISTRIBUTION OF DISTANT SUPERNOVAE AND ITS USE IN PROBING REIONIZATION

ANDREI MESINGER, BENJAMIN D. JOHNSON & ZOLTÁN HAIMAN  
Department of Astronomy, Columbia University, 550 West 120th Street, New York, NY 10027

*Accepted for publication in the ApJ*

## ABSTRACT

We model the number of detectable supernovae (SNe) as a function of redshift at different flux thresholds, making use of the observed properties of local SNe, such as their lightcurves, fiducial spectra, and peak magnitude distributions. We assume that the star-formation rate (SFR) at high redshift traces the formation rate of dark matter halos. We obtain a rate of 0.4–2.3 SNe/arcmin<sup>2</sup>/yr at  $z \gtrsim 5$  at the near infrared (4.5  $\mu\text{m}$ ) flux density threshold of 3 nJy (achievable with the *James Webb Space Telescope (JWST)* in a 10<sup>5</sup>sec integration). In a hypothetical one-year survey, it should be possible to detect up to several thousand SNe per unit redshift at  $z \sim 6$ . We discuss the possible application of such a large sample of distant SNe as a probe of the epoch of reionization. By heating the intergalactic medium (IGM) and raising the cosmological Jeans mass, the process of reionization can suppress star formation in low-mass galaxies. This could have produced a relatively sharp drop in the SNR around the redshift of reionization ( $z_{\text{re}}$ ). We quantify the detectability of this feature in future surveys of distant SNe by varying the redshift and duration of the feature, as well as its impact on the SFR in low-mass halos, which results in different redshifts, widths, and sizes of the drop in the expected SFR. We find that the drop can be detected out to  $z_{\text{re}} \sim 13$ , as long as (i) the reionization history contains a relatively rapid feature which is synchronized over different regions to within  $\Delta z \lesssim 1 - 3$ , (ii) the star-formation efficiency in halos that dominate reionization is  $\epsilon_* \sim 10\%$ , and (iii) reionization significantly suppresses the star formation in low-mass halos. Depending on the details of (i) – (iii), this could be achieved with a survey lasting less than two weeks. Detecting this signature would also help elucidate the feedback mechanism that regulates reionization.

*Subject headings:* cosmology: theory – early Universe – supernovae: general – galaxies: high-redshift – evolution

## 1. INTRODUCTION

The formation of the first astrophysical objects and the subsequent epoch of reionization offer a wealth of insight into the physical processes of the early universe. Two recent developments, revealing the impact of reionization on the Lyman  $\alpha$  absorption spectra of  $z \gtrsim 6$  quasars (Fan et al. 2004; Mesinger & Haiman 2004; Wyithe & Loeb 2004b), and on the temperature/polarization cross-correlation anisotropy in the cosmic microwave background (CMB) radiation (Kogut et al. 2003; Spergel et al. 2003), suggest that reionization history may have been very complex (see, e.g., Haiman 2003 for a review). Various tools designed to probe this epoch have been proposed, relying on upcoming 21-cm surveys (e.g. Madau et al. 1997), high-redshift quasar and galaxy spectra (e.g. Mesinger et al. 2004), high-redshift galaxy surveys (e.g. Barkana & Loeb 2000), GRBs (e.g. Barkana & Loeb 2004a), and more. Nevertheless, there is currently a striking dearth of data or theoretical consensus concerning this important period in the universe’s evolution. Due to the considerable technical challenges associated with such high-redshift observations, some of the most useful objects in the near future are probably going to be some of the brightest and hence easiest to detect, such as bright quasars, GRBs and SNe. Here we make use of the observed properties of local SNe to construct detailed high-redshift SNe rates, obtainable from a future infrared space telescope such as *JWST*. We also show that such a sample of high-redshift SNe could be an invaluable tool in probing the reionization epoch, and the physical feedback mechanism that regulates it.

There have been several previous studies of the expected early SNR. However, these either did not focus on the expected rates at redshifts beyond reionization (e.g. Madau et al. 1998), fo-

cused exclusively on very high- $z$  rates from the first generation of metal-free stars (Wise & Abel 2005), and/or did not address the impact of reionization on the SFR (e.g. Miralda-Escude & Rees 1997; Dahlén & Fransson 1999). Likewise, previous theoretical predictions of the high-redshift SFR (Barkana & Loeb 2000; Bromm & Loeb 2002; Choudhury & Srianand 2002) assumed a fixed degree of suppression due to reionization, matching numerical simulations which did not include self-shielding (Thoul & Weinberg 1996). The main distinctions of the present paper are that we compute the expected SNe rates for the wide range of redshifts within which reionization is expected to have occurred ( $6 \lesssim z_{\text{re}} \lesssim 20$ ), and we allow various degrees of photo-heating feedback. We also supplement the standard halo-based estimates of the SFR with a more elaborate estimate of the corresponding observable SNR, utilizing the observed properties of low- $z$  SNe.

In the presence of an ionizing background radiation, the IGM is photo-heated to a temperature of  $\gtrsim 10,000\text{K}$ , raising the cosmological Jeans mass, which could suppress gas accretion onto small-mass halos (e.g. Efstathiou 1992; Thoul & Weinberg 1996; Gnedin 2000; Shapiro et al. 1994). Reionization is then expected to be accompanied by a drop in the global SFR, corresponding to a suppression of star formation in small halos (i.e. those with virial temperatures below  $T_{\text{vir}} \lesssim 10^4 - 10^5 \text{K}$ ). The size of the drop is uncertain, since the ability of halos to self-shield against the ionizing radiation is poorly constrained at high redshifts. Early work on this subject (Thoul & Weinberg 1996) suggested that an ionizing background would completely suppress star formation in low-redshift “dwarf galaxy” halos with circular velocities  $v_{\text{circ}} \lesssim 35 \text{km s}^{-1}$ , and partially suppress star-formation in halos with  $35 \text{km s}^{-1} \lesssim v_{\text{circ}} \lesssim 100 \text{km s}^{-1}$ .

However, more recent studies (Kitayama & Ikeuchi 2000; Dijkstra et al. 2004) find that at high-redshifts ( $z \gtrsim 3$ ), self-shielding and increased cooling efficiency could be strong countering effects. These calculations, however, assume spherical symmetry, leaving open the possibility of strong feedback for a halo with non-isotropic gas profile, illuminated along a low-column density line of sight (see Shapiro et al. 2004 for a detailed treatment of three-dimensional gas dynamics in photo-heated low-mass halos).

Such a drop in the SFR could be detected in the high-redshift extension of the ‘Lilly – Madau’ diagram (Lilly et al. 1996; Madau et al. 1996), by directly counting faint galaxies (Barkana & Loeb 2000). In practice, the low-mass galaxies susceptible to the reionization suppression are faint and suffer from surface brightness dimming. Whether or not these galaxies will fall above the detection threshold of a deep future survey, so that they can reveal the effect of reionization, depends crucially on the redshift of reionization, the size of the affected galaxies and their typical star-formation efficiencies, as well as the amount of dust obscuration. Alternatively, by analyzing the Lyman  $\alpha$  absorption spectra of SDSS quasars, Cen & McDonald (2002) suggest that we may already have detected a drop in the SFR at  $z \sim 6$ , through the non-monotonic evolution of the mean IGM opacity. In order to improve on this current, low signal-to-noise result, deep, high-resolution spectra of bright quasars would be required from beyond the epoch of reionization at  $z \gtrsim 6$  (this may be possible with *JWST*, see Haiman & Loeb 1999).

Other events that may trace out the early SFR, such as GRBs and SNe, could be better suited to detect the reionization drop, as they are bright, and could be used as tracers of the SFR in arbitrarily faint host galaxies, out to redshifts higher than the host galaxies themselves. This is especially useful, since in hierarchical structure formation scenarios, the characteristic collapse scale decreases with increasing redshift. As a result, the individual galaxies that dominate the ionizing background will likely be undetectable if reionization occurred at high redshift ( $z \gtrsim 10$ ). Unfortunately, while GRBs are bright, they are rare. Based on the expected *Swift* GRB detection rates (e.g. Figure 6 in Mesinger et al. 2005), a drop in the GRB rate associated with reionization could be detected only at very low,  $\sim 1\sigma$ , significance, and only if reionization occurred at  $z_{\text{re}} \lesssim 7 - 10$ . On the other hand, SNe have the benefits of being both very bright (compared to galaxies at the very faint end of the luminosity function), and occurring much more frequently (compared to GRBs).

In summary, *the purpose of this paper is twofold: (i) to construct expected detection rates of high- $z$  SNe in SNe surveys which could be carried out in the future (e.g. with *JWST*); (ii) to quantify the prospects of detecting a reionization feature from such high-redshift SN rates.*

The rest of this paper is organized as follows. In § 2, we present our method for predicting the global SFR and SNR, and estimating the fraction of SNe detectable in a future survey. In § 3.1, we present our estimates for the SNe detection rates. In § 3.2, we estimate the significance at which the reionization-drop in the SNR may be detectable. Finally, we summarize the implications of this work and offer our conclusions in § 4.

Throughout this paper, we assume standard concordance cosmological parameters,  $(\Omega_{\Lambda}, \Omega_{\text{M}}, \Omega_b, n, \sigma_8, H_0) = (0.73, 0.27, 0.044, 1, 0.9, 71 \text{ km s}^{-1} \text{ Mpc}^{-1})$ , consistent with the recent measurements of the power spectrum of CMB temperature anisotropies

by the *Wilkinson Microwave Anisotropy Probe (WMAP)* satellite (Spergel et al. 2003).

## 2. MODELING METHODS

### 2.1. The Intrinsic Star Formation and Supernova Rates

Here we briefly outline our method for obtaining the SFR and the intrinsic SNR, using extended Press-Schechter formalism (EPS) (see Lacey & Cole 1993). The procedure we use to obtain the SFR is based on a relatively standard approach (see, e.g., Mesinger et al. 2005 and references therein). Readers interested in more details are encouraged to consult Mesinger et al. (2005).

We estimate the global SFR density at redshift  $z$  as

$$\dot{\rho}_*(z) = \epsilon_* \frac{\Omega_b}{\Omega_{\text{M}}} \int_{M_{\text{min}}(z)}^{\infty} dM \int_{\infty}^z dz' M \frac{\partial^2 n(> M, z')}{\partial M \partial z'} P(\tau), \quad (1)$$

where  $\epsilon_*$  is the efficiency (by mass) for the conversion of gas into stars,  $M dM (\partial n(> M, z) / \partial M)$  is the mass density contributed by halos with total (dark matter + baryonic) masses between  $M$  and  $M + dM$ ,  $t(z)$  is the age of the universe at redshift  $z$ , and  $P(\tau)$  is the probability per unit time that new stars form in a mass element of age  $\tau \equiv t(z) - t(z')$  (normalized to  $\int_0^{\infty} d\tau P(\tau) = 1$ ). We adopt the fiducial value of  $\epsilon_* = 0.1$  (see, e.g., Cen 2003). Note that the star formation efficiency in minihalos (i.e. halos with virial temperatures below  $10^4 \text{ K}$ ) that contain pristine metal-free gas could be significantly lower than 0.1, as suggested by numerical simulations of the first generation of stars (Abel et al. 2002; Bromm et al. 2002). The expected pre-reionization SNe rates would then lie closer to our  $T_{\text{vir}} \gtrsim 10^4 \text{ K}$  curves prior to reionization (see discussion below), making the detection of the reionization feature significantly more difficult. However, the efficiency is likely to be very sensitive to even trace amounts of metallicity (Bromm et al. 2001), and conditions for star-formation may result in a standard initial mass function (IMF) in gas that has been enriched to metallicities above a fraction  $10^{-4}$  of the solar value. Indeed, it is unlikely that metal-free star-formation in minihalos can produce enough ionizing photons to dominate the ionizing background at reionization (e.g. Haiman et al. 2000; Haiman & Holder 2003; Sokasian et al. 2004). We assume further that star-formation occurs on an extended time-scale, corresponding to the dynamical time,  $t_{\text{dyn}} \sim [G\rho(z)]^{-1/2}$  (Cen & Ostriker 1992; Gnedin 1996):

$$P(\tau) = \frac{\tau}{t_{\text{dyn}}^2} \exp\left[-\frac{\tau}{t_{\text{dyn}}}\right], \quad (2)$$

where  $\rho(z) \approx \Delta_c \rho_{\text{crit}}(z)$  is the mean mass density interior to collapsed spherical halos (e.g. Barkana & Loeb 2001), and  $\Delta_c$  is obtained from the fitting formula in Bryan & Norman (1998), with  $\Delta_c = 18\pi^2 \approx 178$  in the Einstein-de Sitter model. The minimum mass,  $M_{\text{min}}(z)$  in eq. (1), depends on the efficiency with which gas can cool and collapse into a dark matter halo. Prior to reionization and without molecular hydrogen,  $M_{\text{min}}(z)$  corresponds to a halo with virial temperature,  $T_{\text{vir}} \sim 10^4 \text{ K}$ ; with a significant  $\text{H}_2$  abundance, the threshold decreases to  $T_{\text{vir}} \sim 300 \text{ K}$  (Haiman et al. 2000; we use the conversion between halo mass and virial temperature as given in Barkana & Loeb 2001). Post reionization, the Jeans mass is raised, so  $M_{\text{min}}(z)$  could increase. The degree of self-shielding, the ability of the halo gas to cool, as well as the amount of  $\text{H}_2$  present in the high-redshift low-mass halos is uncertain (Dijkstra et al. 2004), and so below we present results for several values of  $M_{\text{min}}(z)$ , which we will henceforth express in terms of  $T_{\text{vir}}(z)$ .

Next, from  $\dot{\rho}_*(z)$  we obtain the intrinsic differential SNR (number of core collapse SNe per unit redshift per year) with

$$\frac{d\dot{N}}{dz} = \eta_{\text{SN}} \frac{1}{1+z} \frac{dV(z)}{dz} \dot{\rho}_*(z), \quad (3)$$

where the factor  $1/(1+z)$  accounts for time dilation,  $dV(z)/dz$  is the comoving volume in our past light cone per unit redshift, and  $\eta_{\text{SN}}$  is the number of SNe per solar mass in stars. For a fiducial Salpeter initial mass function (IMF), we obtain  $\eta_{\text{SN}} \sim 1/180 M_{\odot}^{-1}$ , assuming all stars with masses  $9 M_{\odot} \lesssim M \lesssim 40 M_{\odot}$  become core collapse SNe (Heger et al. 2003). We neglect the lifetime of these high mass stars in determining our SNR; this is a reasonable assumption as the lifetimes (as well as the spread in the lifetimes) are shorter than a unit redshift interval for redshifts of interest. Note that an alternative extreme shape for the IMF, consisting entirely of 100–200  $M_{\odot}$  stars (Abel et al. 2002; Bromm et al. 2002) would yield a similar value for  $\eta_{\text{SN}}$ .

We present our SFR densities (*top panel*) and SNRs (*bottom panel*) in Figure 1. The curves correspond to redshift-independent virial temperature cutoffs of  $T_{\text{vir}} = 300, 10^4, 4.5 \times 10^4$ , and  $1.1 \times 10^5$  K (or circular velocities of  $v_{\text{circ}} = 3, 17, 35$ , and  $55 \text{ km s}^{-1}$ , respectively), top to bottom, spanning the expected range (Thoul & Weinberg 1996; Dijkstra et al. 2004). Also shown are recent results from GOODS (Giavalisco et al. 2004): the bottom points assume no dust correction and the top points are dust corrected according to (Adelberger & Steidel 2000); the statistical error bars lie within the points (Adelberger & Steidel 2000). As there are large uncertainties associated with dust correction, each pair of points (top and bottom) serves to encompass the expected SFR densities.

Our SFRs are consistent with other theoretical predictions (e.g. Somerville et al. 2001; Barkana & Loeb 2000; Bromm & Loeb 2002), as well as other recent estimates from the Hubble Ultra Deep Field (Bunker et al. 2004) and the FORS Deep Field on the VLT (Gabasch et al. 2004), after they incorporate a factor of 5–10 increase in the SFR (Adelberger & Steidel 2000) due to dust obscuration. Furthermore, we note that our SNRs, which at  $z \gtrsim 5$  yield 0.3 – 2 SNe per square arcminute per year, are in good agreement with the  $\sim 1$  SN per square arcminute per year estimated by Miralda-Escude & Rees (1997) by requiring that high-redshift SNe produce a mean metallicity of  $\sim 0.01 Z_{\odot}$  by  $z \sim 5$ . Note, however, that the rates we obtain are significantly higher (by a factor of  $\sim 60 - 2000$  at  $z \sim 20$ ) than those recently found by Wise & Abel (2005). The reason for this large difference is that Wise & Abel consider star-formation only in minihalos, and they assume a very low star-formation efficiency of a single star per minihalo, as may be appropriate for star-formation out of pristine (metal-free) gas in the first generation of minihalos (Abel et al. 2002; Bromm et al. 2002). In contrast, we assume an efficiency of  $\epsilon_* = 0.1$ , which may be more appropriate for star-formation in pre-enriched gas that dominates the SFR just prior to reionization (including star-formation in minihalos).

As mentioned above, by increasing the cosmological Jeans mass, reionization is expected to cause a drop in the SFR (and hence the SNR), with the rates going from the horizontally striped region in Figure 1 at  $z > z_{\text{re}}$  to the vertically striped region at  $z < z_{\text{re}}$ .

The redshift width of this transition is set by a combination of large-scale cosmic variance, radiative transfer, and feedback effects. For the majority of the paper, we use  $\Delta z_{\text{re}} \sim 1$  as a rough indicator of the width of the transition we are analyzing. We distinguish between “reionization” and a “reionization

feature”, and use  $\Delta z_{\text{re}}$  as an indicator of the width of the later. Even with an extended reionization history ( $\Delta z \sim 10$ ), fairly sharp ( $\Delta z_{\text{re}} \lesssim 3$ ) features are likely. We postpone a more detailed discussion until § 3.2.4.

The other important factor determining the usefulness of the method proposed here is the factor by which the SFR drops during the reionization epoch. The size of this drop is mediated by the effectiveness of self-shielding and gas cooling during photo-heating feedback: i.e. on whether or not the star-formation efficiency is significantly suppressed in those halos that dominate the SFR and SNR immediately preceding the reionization epoch. Given the uncertainties about this feedback discussed above, we will consider a range of possibilities below, parameterized by the modulation in the virial temperature threshold for star-formation during reionization.

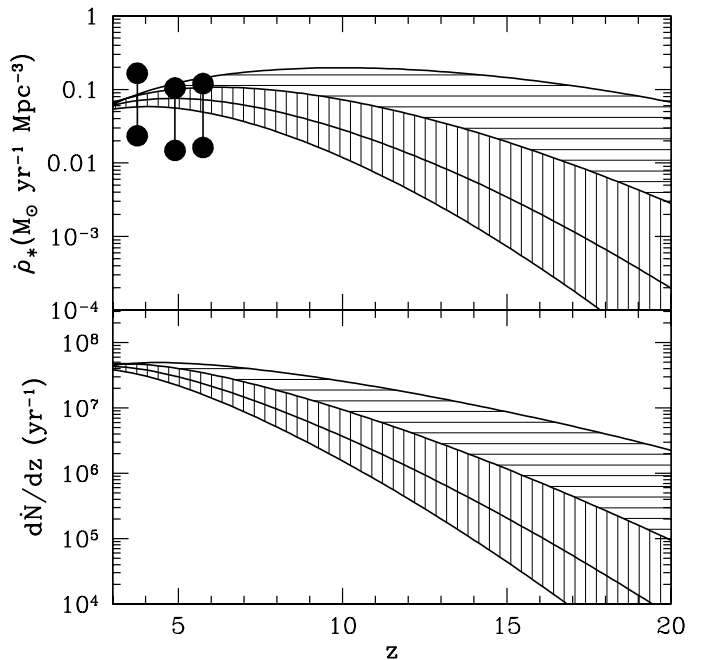


FIG. 1.— *Upper Panel*: SFR densities obtained from our model. The curves (*top to bottom*) correspond to different lower cutoffs on the virial temperatures of star-forming halos,  $T_{\text{vir}} \gtrsim 300, 10^4, 4.5 \times 10^4$ , and  $1.1 \times 10^5$  K (corresponding to circular velocity thresholds of  $v_{\text{circ}} \gtrsim 3, 17, 35$ , and  $55 \text{ km s}^{-1}$ ). Dots indicate results from GOODS (Giavalisco et al. 2004): the lower set of points assume no dust correction, while the upper set of points are dust corrected; statistical  $1\text{-}\sigma$  error bars lie within the points. The lines connecting each pair of points span the expected range of SFR densities. *Lower Panel*: the SNR densities accompanying the SFR densities in the top panel. A reionization feature at redshift  $z_{\text{re}}$  is expected to be evidenced by a drop in the above rates, with rates changing from the horizontally striped region at  $z > z_{\text{re}}$  to the vertically striped region at  $z < z_{\text{re}}$ , within a transition period lasting for  $\Delta z_{\text{re}}$ .

## 2.2. High Redshift SNe in Future Surveys

Given the intrinsic star-formation and SN rates, our next task is to estimate the number of SNe that could be revealed by a future SNe search. In general, the number of SNe per unit redshift,  $dN_{\text{exp}}/dz$ , that are bright enough to be detectable in an exposure of duration  $t_{\text{exp}}$  can be expressed as

$$\frac{dN_{\text{exp}}}{dz} = \frac{d\dot{N}}{dz} \int_0^{\infty} f_{\text{SN}}(> t_{\text{obs}}, z) dt_{\text{obs}}, \quad (4)$$

where  $(d\dot{N}/dz)dt_{\text{obs}}$  is the number of SNe which occurred between  $t_{\text{obs}}$  and  $t_{\text{obs}} + dt_{\text{obs}}$  ago (per unit redshift; note that the

global mean SNR will evolve only on the Hubble expansion time–scale, and can be considered constant over several years), and  $f_{\text{SN}}(> t_{\text{obs}}, z)$  is the fraction of SNe which remain visible for at least  $t_{\text{obs}}$  in the observed frame. Then the total number of SNe detected in a survey of duration  $t_{\text{surv}}$  is

$$N_{\text{surv}} = \frac{t_{\text{surv}}}{2 t_{\text{exp}}} \frac{\Delta\Omega_{\text{FOV}}}{4\pi} N_{\text{exp}}, \quad (5)$$

where  $\Delta\Omega_{\text{FOV}}$  is the instrument’s field of view, and  $t_{\text{surv}}/(2t_{\text{exp}})$  is the number of fields which can be tiled in the survey time,  $t_{\text{surv}}$  (we add a factor of 1/2 to allow for a second pair of filters to aid in the photometric redshift determination; note that this provides for imaging in 4 different *JWST* bands; see discussion below). Note also that equation (5) is somewhat idealized, in that it assumes continuous integration for the duration of the survey, and e.g., does not account for time required to slew the instrument to observe different fields. In principle, each field has to have repeated observations (to detect SNe by their variability), and therefore any dedicated survey should target fields that have already been observed. Furthermore, a long, dedicated program may not be necessary, because the effect could be detected with relatively few fields (at least under optimistic assumptions; see discussion below), and several fields with repeated imaging (separated by  $> 1 - 2$  years) may already be available from other projects; these fields can then be used for the SN search.

Additionally, it might prove useful to consider the luminosity of a SN host galaxy as a means of biasing the sample towards the small mass halos which are most susceptible to the reionization suppression. Ignoring SNe which originate in galaxies above a certain threshold luminosity at a given redshift could limit the sample to those small halos which are most affected by reionization, and hence decrease the “noise” component in the reionization signal (e.g. eq. (6)). If there turns out to be strong correlation between SN type and host halo properties (e.g. due to metallicity), then, in principle, such correlations can be empirically discovered and used to further narrow the SN sample to those most susceptible to feedback - even if the expected correlation cannot be predicted ab-initio.

In general,  $f_{\text{SN}}(> t_{\text{obs}}, z)$  in equation (4), i.e. the fraction of SNe which remain visible for at least  $t_{\text{obs}}$ , depends on (i) the properties of the SN, in particular their peak magnitude and lightcurve, and the distribution of these properties among SNe, and (ii) on the properties of the telescope, such as sensitivity, spectral coverage, and field of view. In the next two subsections, we discuss our assumptions and modeling of both of these in turn.

### 2.2.1. Empirical Calibration of SN Properties

At each redshift, we run Monte-Carlo simulations to determine  $f_{\text{SN}}(> t_{\text{obs}}, z)$  in equation (4). We use the observed properties of local core-collapse SNe (CCSNe) in estimating  $f_{\text{SN}}(> t_{\text{obs}}, z)$ . For the high redshifts of interest here, we only consider core collapse SNe of Type II. SNe resulting from the collapse of Chandreshekar–mass white dwarfs (Type Ia) are expected to be extremely rare at high redshifts ( $z \gtrsim 6$ ), as the delay between the formation of the progenitor and the SN event ( $\gtrsim 1$  Gyr; Strolger et al. 2004) is longer than the age of the universe at these redshifts. Local core CCSNe come in two important varieties, types IIP and IIL, differentiated by their lightcurve shapes. We ignore the extremely rare additional CCSN types, e.g Type IIn and IIb, which appear to have significant interaction with circumstellar material and constitute less than 10% of

all CCSNe. Type Ib/c, which may or may not also result from core collapse, have luminosities and light-curves that are similar to Type IIL and occur less frequently. While the relative numbers of Type IIP and Type IIL SNe are not known even for nearby SNe, recent estimates imply that they are approximately equal in frequency (Cappellaro et al. 1997). We therefore assume that 50% of the high-redshift SNe are Type IIP and 50% are Type IIL.

CCSNe result from the collapse of the degenerate cores of high-mass stars. The luminosity of CCSNe is derived from the initial shock caused by the core-collapse which ionizes material and fuses unstable metal isotopes (see Leibundgut & Suntzeff (2003) and references therein for a more detailed description of SN lightcurves). In the early stages of the SN, the shock caused by the core collapse breaks out from the surface of the progenitor (typically high mass red giants), resulting in a bright initial peak in the light curve that lasts less than a few days in the rest-frame of the SN. As the shock front cools, the SN dims. However, the SN may then reach a plateau of constant luminosity in the light curve, believed to be caused by a wave of recombining material (ionized in the shock) receding through the envelope. The duration and strength of this plateau depends on the depth and mass of the progenitor envelope, as well as the explosion energy, with those SNe exhibiting a strong plateau classified as Type IIP. A typical plateau duration is  $\lesssim 100$  rest-frame days (Patat et al. 1994). In Type IIL SNe, this plateau is nearly non-existent, and the lightcurve smoothly transitions from the rapid decline of the cooling shock to a slower decline where the luminosity is powered by the radioactive decay of metals in the SN nebula. After the plateau, Type IIP SNe also enter this slowly declining ‘nebular’ phase.

These observationally determined behaviors have been summarized in a useful form as lightcurve templates in Doggett & Branch (1985). We use these template lightcurves in determining  $f_{\text{SN}}(> t_{\text{obs}}, z)$ , and normalize the lightcurves using gaussian-distributed peak magnitudes (i.e. log-normally distributed in peak flux) determined by Richardson et al. (2002) from a large sample of local Type IIP and Type IIL SNe (see Table 1). We perform the Monte-Carlo simulations with both the dust corrected, and dust uncorrected values in Richardson et al. (2002), since the dust production history of the early universe is poorly understood and is essentially unconstrained empirically.

We use a combined high-resolution HST STIS + ground-based spectrum of the Type IIP supernova SN1999em (the ‘November 5th’ spectrum of Baron et al. 2000) as the template SN spectrum in order to obtain  $K$ -corrections (with the Doggett & Branch 1985 lightcurves given in the restframe  $B$  filter). This spectrum was obtained within 10 days of maximum light, i.e. during the initial decline of the SN brightness, and has been dereddened by  $A_V = 0.3$  mag (Baron et al. 2000; Hamuy et al. 2001). While the spectrum, and hence the  $K$ -corrections, of SNe evolve during the lightcurve, this effect is not strong for the wavelengths of interest (Patat et al. 1994), especially since the lightcurve template we use is well matched to the wavelengths being probed by the observations we consider below (leading to small  $K$ -corrections). We have also used this Type IIP SN template spectrum to calculate  $K$ -corrections for Type IIL SNe. This is necessary due to the lack of restframe UV spectra of Type IIL SNe that can be combined with optical spectra, and justifiable because the  $K$ -corrections are relatively small and the broadband colors of both Type IIP and IIL SNe (a measure of the spectral shape that determines the  $K$ -corrections) are sim-

ilar, at least in the optical (Patat et al. 1994). Note that we assume that very-high redshift core-collapse SNe are similar to local SNe in their spectra, peak luminosities, and temporal evolution. However, these assumption do not significantly impact our conclusions below, as long as (i) the average properties of the SNe do not change *rapidly* at high redshift (which could mimic the reionization drop), (ii) they do not become preferentially underluminous (which would make high- $z$  SNe less detectable, lowering the statistical confidence at which the reionization drop is measured), and (iii) the detection efficiency does not change rapidly with redshift (e.g. due to instrument parameters or spectral lines).

TABLE 1

MEANS AND STANDARD DEVIATIONS OF THE ADOPTED PEAK ABSOLUTE MAGNITUDES. VALUES ARE TAKEN FROM RICHARDSON ET AL. (2002). NOTE: AN  $M_B = -17$  SN WOULD BE DETECTABLE OUT TO  $z \approx 8.2$  AT THE FLUX THRESHOLD OF 3 nJy AT 4.5  $\mu\text{m}$ .

SN Type	Corrected for Dust		Not Corrected for Dust	
	$\langle M_B \rangle$	$\sigma$	$\langle M_B \rangle$	$\sigma$
IIP	-17.00	1.12	-16.61	1.23
IIL	-18.03	0.9	-17.80	0.88

In order to use the method outlined above to probe reionization, the SN redshifts must also be known to an accuracy of  $\Delta z \lesssim 1$ . SN redshifts can be determined via spectroscopy of either the SN itself, or of the host galaxy. However, as we have already noted, the host galaxies may only be marginally detectable even in imaging, and the SNe may be too faint for anything other than extremely low resolution spectroscopy. We present here only a very brief example of the possibility of obtaining redshifts from the extremely low resolution ( $\lambda/\Delta\lambda \sim 5$ ) spectra provided by multiband imaging: a complete investigation of this possibility is warranted, but is beyond the scope of this paper.

To the extent that Type II SNe spectra can be represented as a sequence of blackbodies of different temperatures (e.g. Dahlén & Fransson 1999) photometric redshifts will be impossible to obtain without information about the SN epoch, since temperature and redshift would be degenerate. However, local Type IIP SNe show significant deviations from a blackbody in the UV ( $\lambda < 3500\text{\AA}$ ) due to metal-line blanketing in the SN photosphere, providing spectral signatures that could be used as redshift indicators, depending on their strength. In Figure 2, we show the evolution with redshift of the infrared colors (in bands accessible with *JWST*; see below) of our template SN spectrum, compared with the color evolution of a blackbody. The figure shows that the template spectrum deviates significantly from a blackbody. If the spectrum of the SN is always the same as the template spectrum, then there are good prospects for obtaining photometric redshifts for these SNe, at least in the redshift range  $z = 7 - 13$ . While the figure shows that multiple redshifts may be possible at fixed observed colors, the degenerate solutions would correspond to  $z > 16$  SNe; contamination from such high redshift will be mitigated by the fact that these SNe are likely to be too faint to be detected. Of course, more detailed studies of the UV behavior of local SNe, especially their variety and spectral evolution, will be necessary to confirm the possible use of photometric redshifts.

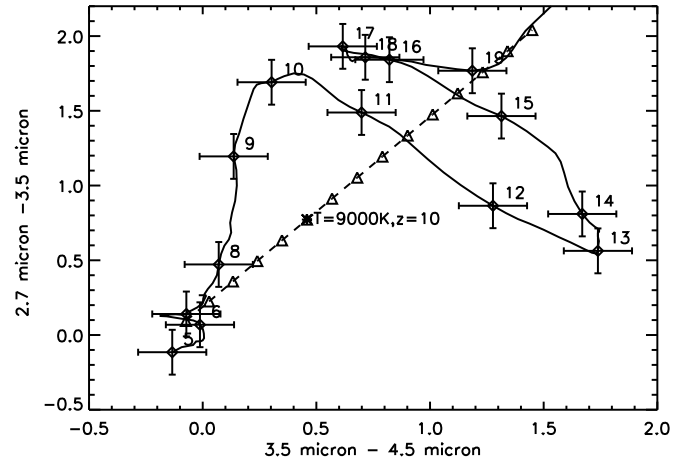


FIG. 2.— Infrared colors of a Type II SN as a function of its redshift. *Solid curve*: The template spectrum of the text, from the Type IIP SN 1999em. Diamonds are placed at intervals of  $\Delta z = 1$ , labeled with the redshift. Error bars of 0.15 mag are shown to give a sense of the photometric errors that may be expected, excluding the many possible systematic effects. *Dashed curve*: The colors of a blackbody at different redshifts (temperatures). The asterisk marks the color of a 9000K blackbody at  $z = 10$ , triangles are at intervals of  $\Delta z = 1$  (or at a constant redshift but with a corresponding different temperature)

### 2.2.2. SNe Detectability and Survey Parameters

As a specific example for the number of detectable SNe in a future sample, we consider observations by *JWST*, a 6m diameter space telescope, scheduled for launch in 2013. Similar constraints could be delivered by the *Joint, Efficient Dark-energy Investigation (JEDI)*<sup>1</sup> (Wang et al. 2004), a proposed instrument which will require a  $\sim 100$  times longer integration time to reach the same detection threshold, but has a  $\sim 100$  times larger FOV. The relevant instrument on *JWST* is NIRcam,<sup>2</sup> a near-infrared imaging detector with a FOV of  $2.3' \times 4.6'$ . A field can be observed in two filters simultaneously. NIRcam will have five broadband filters (with resolution  $\lambda/\Delta\lambda \sim 5$ ). We model the filter response as tophat functions with central wavelengths of 1.5, 2.0, 2.7, 3.5, and 4.5  $\mu\text{m}$ . For concreteness, below we will present results only for the 4.5 and 3.5  $\mu\text{m}$  filters, since they are the longest-wavelength *JWST* bands; however, we allow time for imaging in two other bands, if needed for photometric redshift determinations. The current estimate of the *JWST* detection threshold at 4.5  $\mu\text{m}$  is  $\gtrsim 3$  nJy for a 10  $\sigma$  detection and an exposure time of  $10^5$  s. The 3.5  $\mu\text{m}$  band is more sensitive, with a detection threshold of  $\gtrsim 1$  nJy for a 10  $\sigma$  detection and an exposure time of  $10^5$  s.

We show our results for  $f_{\text{SN}}(> t_{\text{obs}}, z)$  in Figure 3. The solid curves correspond to  $z = 7$ , the dashed curves correspond to  $z = 10$ , and the dotted curves correspond to  $z = 13$ . In each panel, the top set of curves assumes a flux threshold of 3 nJy (or an exposure time of  $t_{\text{exp}} = 10^5$  seconds in the 4.5  $\mu\text{m}$  band), and the bottom set assumes 9.5 nJy ( $t_{\text{exp}} = 10^4$  seconds in the 4.5  $\mu\text{m}$  band, background dominated). The top panel further assumes no dust extinction, while in the bottom panel, we adopt the same dust extinction as in the low redshift sample (Richardson et al. 2002). Understandably, the distributions get wider as redshift increases (due to time dilation), but the total visible fraction,  $f_{\text{SN}}(> 0, z)$ , gets smaller (due to the increase in

<sup>1</sup><http://jedi.nhn.ou.edu/>

<sup>2</sup>See <http://ircamera.as.arizona.edu/nircam> for further details.

luminosity distance). The double bump feature in some of the curves corresponds to the plateau of Type IIP SNe lightcurves discussed above.

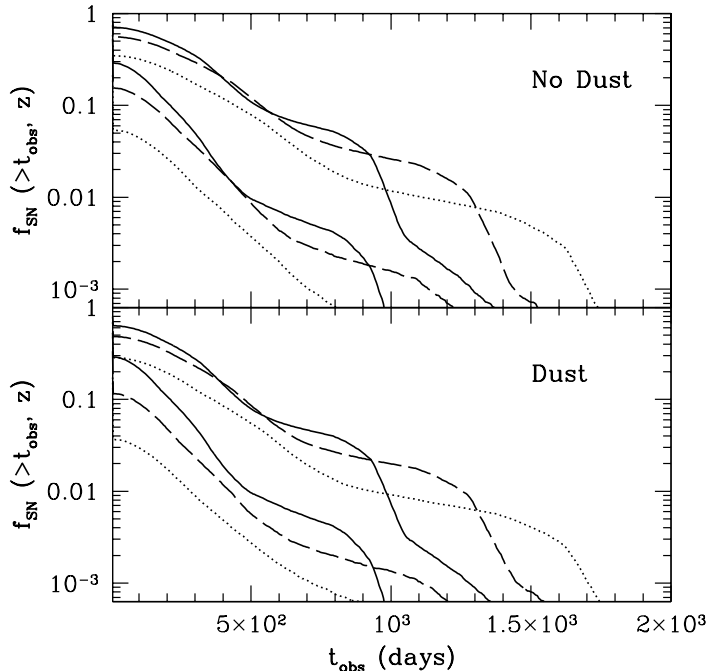


FIG. 3.— Fraction of SNe which remains visible for an observed duration of  $t_{\text{obs}}$  or longer. The curves correspond to SN redshifts of  $z = 7$  (solid curve),  $z = 10$  (dashed curve), and  $z = 13$  (dotted curve). In each panel, the top set of curves assumes a flux threshold of 3 nJy (exposure time of  $t_{\text{exp}} = 10^5$  s with the  $4.5 \mu\text{m}$  *JWST*), and the bottom set assumes 9.5 nJy ( $t_{\text{exp}} = 10^4$  s). The top panel assumes no dust extinction, while the bottom panel assumes the same dust extinction as observed within the low redshift sample (Richardson et al. 2002).

As seen in Figure 3, most of the supernovae that are bright enough to be visible at all, will remain visible for up to  $\sim 1 - 2$  years. Hence, in order to catch the most SNe, it will be necessary to have repeat observations of the SN survey fields a few years apart, to insure that most of the observed SNe will be identified as new sources or sources that have disappeared. A time between observations that is comparable to or larger than the SN duration will be the optimal strategy for detecting the most SNe (Nemiroff 2003). Note that we ignore the time required to collect reference images, since observations conducted for other programs will likely provide a sufficient set of such reference images. However, as shown in equation (5), we allow time for the field to be imaged in four different bands, to aid in photometric redshift determination.

To be more explicit, we find that in order to obtain the largest number of high-redshift SNe, in general it is a more efficient use of *JWST*'s time to 'tile' multiple fields rather than 'stare' for extended periods of time ( $\gtrsim 10^4$  s) at the same field (Nemiroff 2003). This is because of strong time dilation at these redshifts. As can be seen from Figure 3, most detectable SNe will remain above the detection threshold for several months, even assuming  $10^4$  s integration times. Also evident from Figure 3 is that the increase in the total visible fraction of SNe going from  $t_{\text{exp}} = 10^4$  s to  $t_{\text{exp}} = 10^5$  s, is less than the factor of 10 increase in exposure time. As a result, a fiducial 1-yr *JWST* survey would therefore detect more SNe using  $t_{\text{exp}} = 10^4$  s than using  $t_{\text{exp}} = 10^5$  s (see Figures 4a and 5a). Understandably, this conclusion does not hold for very high-redshifts,  $z \gtrsim 14$ , where

SNe are extremely faint, and require very long exposure times to be detectable. However, even with such long exposure times, very few SNe will be detectable at these large redshifts, rendering the use of longer exposure times unnecessary.

### 3. RESULTS AND DISCUSSION

#### 3.1. SNe Detection Rates

The number of SNe that could be detectable in putative future surveys are shown in Figures 4a and 5a. The curves correspond to the same virial temperature cutoffs for star-forming halos as in Figure 1. Solid lines assume no dust obscuration; dashed lines include a correction for dust obscuration as discussed above. Figure 4a shows results assuming flux density thresholds of 9.5 nJy (or  $t_{\text{exp}} = 10^4$  s with the  $4.5 \mu\text{m}$  *JWST* filter) (top panel) and 3 nJy ( $t_{\text{exp}} = 10^5$  s) (bottom panel). Figure 5a shows results with the  $3.5 \mu\text{m}$  filter assuming equivalent exposure times: flux density thresholds of 3.2 nJy ( $t_{\text{exp}} = 10^4$  s with the  $3.5 \mu\text{m}$  *JWST* filter) (top panel) and 1 nJy ( $t_{\text{exp}} = 10^5$  s) (bottom panel). The right vertical axis displays the number of SNe per unit redshift per FOV ( $2.3' \times 4.6'$ ); the left vertical axis shows the number of SNe per unit redshift in a fiducial 1-year survey. As mentioned above, reionization should be marked by a transition from the region bounded by the top two solid curves to the region enclosed by the bottom three solid curves (or the analog with the dashed curves if dust is present at the time of reionization).

We note that our expected rates are somewhat higher than those in Dahlén & Fransson (1999), a previous study which included SNe lightcurves and spectra in the analysis. For example, we find 4 – 24 SNe per field at  $z \gtrsim 5$  in the  $4.5 \mu\text{m}$  filter with  $t_{\text{exp}} = 10^5$  s, compared to  $\sim 0.7$  SNe per field at  $z \gtrsim 5$  obtained by Dahlén & Fransson (1999) (after updating their *JWST* specifications to the current version). However, they use SFRs extrapolated from the low-redshift data available at the time, which are not a good fit to recent high- $z$  SFR estimates (Gialisco et al. 2004; Gabasch et al. 2004; Bunker et al. 2004), and are lower than our  $z \gtrsim 5$  SFRs by a factor of 6 – 40.<sup>3</sup> Taking this factor into account, their procedure yields 4 – 27 SNe per field at  $z \gtrsim 5$ , which is in excellent agreement with our estimate of 4 – 24 SNe per field at  $z \gtrsim 5$ .

#### 3.2. Detecting Reionization Features

To quantify the feasibility of detecting the reionization feature, we assume a Poisson S/N,

$$S/N = \sqrt{n_{\text{field}}} \frac{\langle N_{\text{pre}} \rangle - \langle N_{\text{post}} \rangle}{\sqrt{\langle N_{\text{pre}} \rangle + \langle N_{\text{post}} \rangle}}, \quad (6)$$

where  $n_{\text{field}}$  is the number of *JWST* fields, and  $\langle N_{\text{pre}} \rangle$  and  $\langle N_{\text{post}} \rangle$  are the number of observable SNe per field per unit redshift pre and post reionization, averaged over  $z_{\text{re}} < z < z_{\text{re}} + \Delta z_{\text{re}}$  and  $z_{\text{re}} - \Delta z_{\text{re}} < z < z_{\text{re}}$ , respectively. In our fiducial model we take  $\Delta z_{\text{re}} = 1$ , but below we also investigate the impacts of a larger value of  $\Delta z_{\text{re}}$ . Equation (6) yields a simple figure of merit that does not distinguish between the theoretical means of the distributions we generate and the future observational samples which will have to be interpreted as numbers drawn from distributions with unknown means. Likewise, simple  $\sqrt{N}$  errors are underestimates for small  $N$ . However, we have verified that at our

<sup>3</sup>The possibility that the SFR in a ‘Lilly-Madau diagram’ remains flat, or even increases, at redshifts  $z \gtrsim 5$ , owing to star-formation in early, low-mass halos, is also expected theoretically (see, e.g., Fig.1 in Bromm & Loeb 2002 and associated discussion).

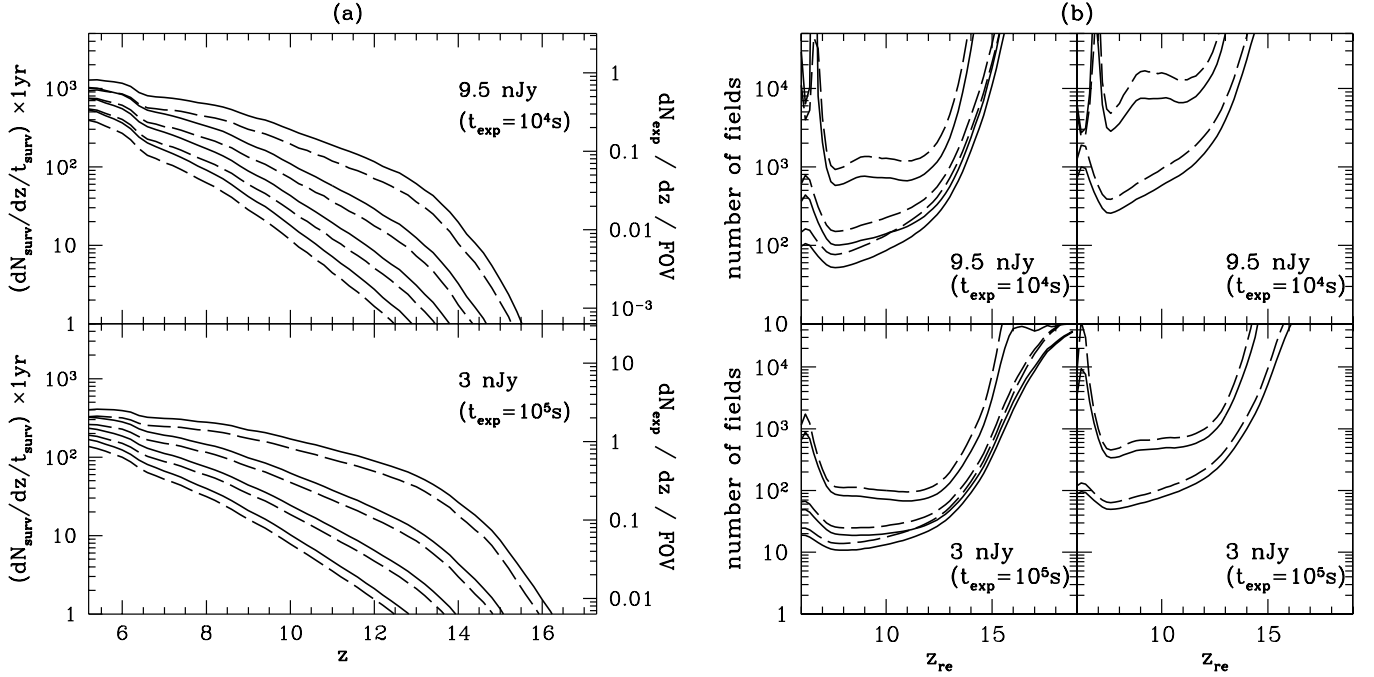


FIG. 4. — (a) Number of high-redshift SNe detectable with the  $4.5 \mu\text{m}$  JWST filter. The curves correspond to the same virial temperature cutoffs as in Figure 1. Solid curves assume no dust obscuration; dashed curves adopt dust obscuration in the same amount as observed in the low redshift SNe sample. The figure shows results assuming flux density thresholds of 9.5 nJy (or  $t_{\text{exp}} = 10^4$  s with JWST) (top panel) and 3 nJy (or  $t_{\text{exp}} = 10^5$  s with JWST) (bottom panel). The right vertical axis displays the number of SNe per unit redshift per field; the left vertical axis shows the number of SNe per unit redshift found in  $t_{\text{surv}}/(2t_{\text{exp}})$  such fields (i.e. the differential version of eq. (5) with  $t_{\text{surv}} = 1$  yr). Reionization should be marked by a transition from the region bounded by the top two solid curves to the region enclosed by the bottom three solid curves (or the analog with the dashed curves if dust is present at the time of reionization). (b) Number of  $2.3' \times 4.6'$  JWST fields. The top panels assume  $t_{\text{exp}} = 10^4$  s; bottom panels assume  $t_{\text{exp}} = 10^5$  s. *Left:* Reionization drops in the SNR analogous to  $T_{\text{vir}} \gtrsim 300 \text{ K} \rightarrow 10^4 \text{ K}$ ,  $T_{\text{vir}} \gtrsim 300 \text{ K} \rightarrow 4.5 \times 10^4 \text{ K}$ , and  $T_{\text{vir}} \gtrsim 300 \text{ K} \rightarrow 1.1 \times 10^5 \text{ K}$ , (top to bottom). *Right:* Reionization drops in the SNR analogous to  $T_{\text{vir}} \gtrsim 10^4 \text{ K} \rightarrow 4.5 \times 10^4 \text{ K}$ , and  $T_{\text{vir}} \gtrsim 10^4 \text{ K} \rightarrow 1.1 \times 10^5 \text{ K}$ , (top to bottom).

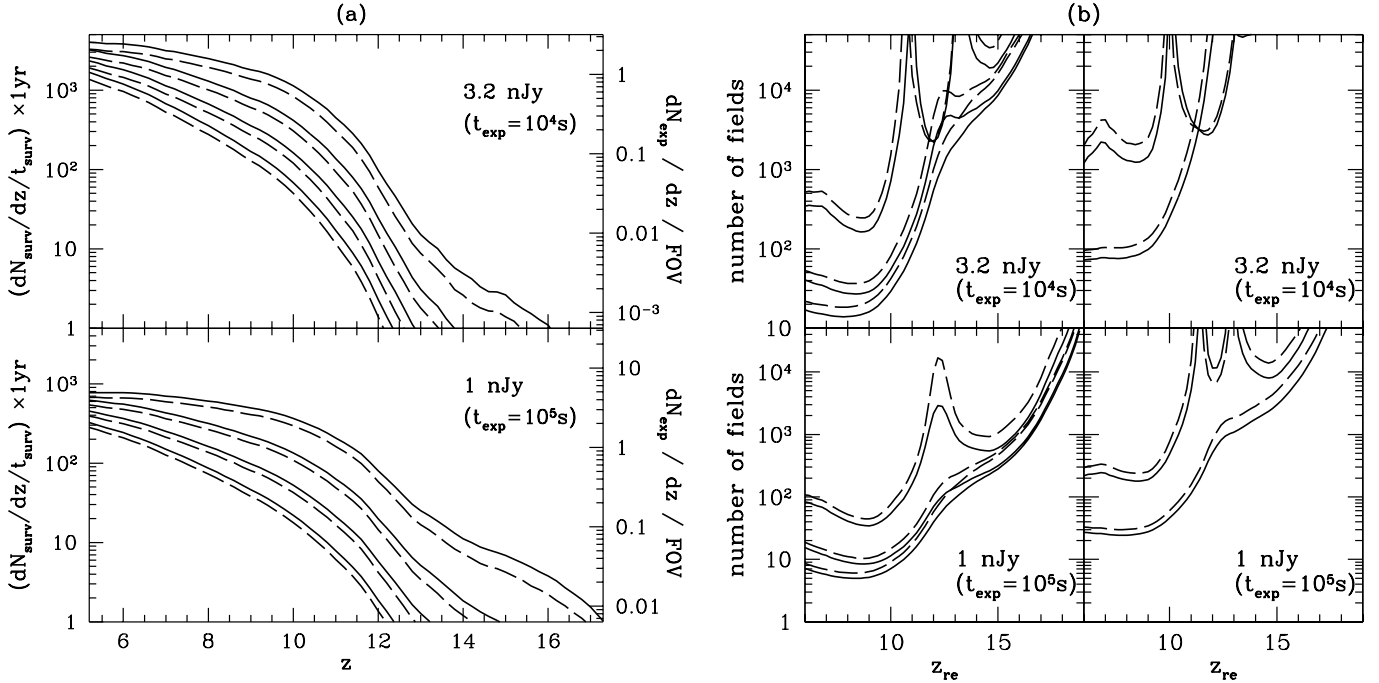


FIG. 5. — Same as Figure 4, but with the  $3.5 \mu\text{m}$  filter, instead of the  $4.5 \mu\text{m}$  one. Note that we present results for comparable exposure times, hence the sensitivity thresholds are three times lower than in Figure 4, due to the disparate sensitivities of the  $3.5 \mu\text{m}$  and  $4.5 \mu\text{m}$  filters.

chosen limiting value of  $S/N \gtrsim 3$ , these issues have little impact on the results. A full statistical treatment (e.g. comparing redshift distribution of counts with a Fisher matrix technique; Holder et al. 2001) is beyond the scope of this paper, and would be of little value given the uncertainties in our estimates. However, we note that the statistics could be improved by combining several (e.g.  $\Delta z = 0.5$  wide) bins prior to and following reionization, or by applying the null-hypothesis of a smoothly evolving SNR directly to the unbinned table of the observed SNe (Holder et al. 2001).

In Figures 4b and 5b, we plot the number of 4.5 and 3.5  $\mu\text{m}$  *JWST* fields, respectively, required to detect the reionization feature at  $z_{\text{re}}$  with a  $S/N \gtrsim 3$ . Solid curves correspond to no dust obscuration; dashed curves include dust corrections. The top panels assume  $t_{\text{exp}} = 10^4$  s; bottom panels assume  $t_{\text{exp}} = 10^5$  s. The left panels show the results assuming that reionization modifies the virial temperature cutoff as  $T_{\text{vir}} \gtrsim 300 \text{ K} \rightarrow 10^4 \text{ K}$ ,  $T_{\text{vir}} \gtrsim 300 \text{ K} \rightarrow 4.5 \times 10^4 \text{ K}$ , and  $T_{\text{vir}} \gtrsim 300 \text{ K} \rightarrow 1.1 \times 10^5 \text{ K}$ , from top to bottom. The right panels show results under the less pronounced transitions of  $T_{\text{vir}} \gtrsim 10^4 \text{ K} \rightarrow 4.5 \times 10^4 \text{ K}$ , and  $T_{\text{vir}} \gtrsim 10^4 \text{ K} \rightarrow 1.1 \times 10^5 \text{ K}$ , from top to bottom. To obtain the corresponding number of necessary SNe, one can multiply the number of required fields in Figures 4b and 5b with the corresponding number of SNe per unit redshift per field in Figures 4a and 5a, respectively. Typically, the detection of the reionization drop with  $S/N \gtrsim 3$  requires at least  $\langle N_{\text{pre}} \rangle \gtrsim 10$  SNe.

The relative flatness of most of the curves in Figures 4b and 5b over the ranges  $7 \lesssim z_{\text{re}} \lesssim 13$  and  $6 \lesssim z_{\text{re}} \lesssim 10$ , respectively, is due to the fact that even though the number of detections decreases with increasing redshift (making the detection of the reionization drop more difficult), the separation between the various suppression curves increases (making the detection of the reionization drop easier). We note from the figures that detecting the reionization drop in the SNe distributions constructed from the 3.5  $\mu\text{m}$  filter is more efficient (requires fewer comparable fields) than using the 4.5  $\mu\text{m}$  filter at redshifts  $6 \lesssim z_{\text{re}} \lesssim 10$ . At redshifts larger than  $z_{\text{re}} \sim 10$ , the 4.5  $\mu\text{m}$  filter becomes more efficient, and can be used to detect the reionization drop out to  $z_{\text{re}} \lesssim 15$  in a 1 year survey, in the most optimistic scenario. However, such conclusions about SNe at redshifts as high as  $z_{\text{re}} \gtrsim 13$ –15 are highly uncertain: (i) there could be an intrinsic physical cut-off to the bright-end tail of the SNe luminosity distributions, drastically reducing the number of detectable SNe at very high redshifts, and/or (ii) detections in the 3.5  $\mu\text{m}$  band, in addition to the 4.5  $\mu\text{m}$  band, could be necessary for photometric redshift determination (see § 2.2.1), which could further reduce the number of very high redshift SNe with accurate redshift determinations.

In the most optimistic scenario we considered (with the threshold for star formation raised from  $T_{\text{vir}}(z > z_{\text{re}}) \gtrsim 300 \text{ K}$  to  $T_{\text{vir}}(z < z_{\text{re}}) \gtrsim 1.1 \times 10^5 \text{ K}$ ), corresponding to maximum photo-heating feedback (abundant  $\text{H}_2$  cooling and no self-shielding), the drop can be detected with just 8 (3.5  $\mu\text{m}$ ) fields over the range  $6 \lesssim z_{\text{re}} \lesssim 10$  and 20 (4.5  $\mu\text{m}$ ) fields over the range  $6 \lesssim z_{\text{re}} \lesssim 13$  with  $t_{\text{exp}} = 10^5$  s. Using shorter exposures, it can be detected with 20 (3.5  $\mu\text{m}$ ) fields over the range  $6 \lesssim z_{\text{re}} \lesssim 10$  and 100–300 (4.5  $\mu\text{m}$ ) fields over the range  $6 \lesssim z_{\text{re}} \lesssim 13$  with  $t_{\text{exp}} = 10^4$  s. Less optimistic scenarios can still allow for a detection of the reionization drop with only tens of fields. However, a reionization feature at  $z_{\text{re}} \gtrsim 15$ , would require  $\gtrsim 1000$  fields in order for the associated drop to be detected.

In the most pessimistic scenario (with the threshold changing

from  $T_{\text{vir}} \gtrsim 10^4 \text{ K} \rightarrow 10^4 \text{ K}$ ), corresponding to very strong self-shielding and no  $\text{H}_2$  at reionization (i.e. the complete absence of any photo-heating feedback), reionization would not affect the SNR and could not be detected. Nevertheless, if a sharp reionization feature is detected independently (through  $\text{Ly}\alpha$  absorption spectra of galaxies or quasars, 21-cm signatures, or CMB anisotropies), the lack of a detected drop in the SNR would provide valuable evidence that low-mass halos can withstand the effects of photo-ionization heating. Note that without a complementing detection of a sharp reionization feature, one can not distinguish between a very smooth, gradual reionization and an absence of photo-heating feedback.

Finally, we comment on the origin of the spike at  $z_{\text{re}} \sim 6$  in the curves in Figure 4b. Apparently, the detection of the reionization feature in the 4.5  $\mu\text{m}$  band at  $z_{\text{re}} \sim 6$ –7 has an additional difficulty. This is caused by a combination of two effects: (i) the decreasing separation between the observable SNe distributions (as seen in Figure 4a) at lower redshifts, and (ii) a large-equivalent-width  $\text{H}\alpha$  emission line in the spectrum of our template SNe, SN1999em, at the rest frame wavelength  $\lambda_{\text{H}\alpha} \approx 6563 \text{ \AA}$ . (The latter effect also produces the slight bump in the curves in Figure 4a at the redshift in which the 4.5  $\mu\text{m}$  filter probes the line,  $z_{\text{H}\alpha, 4.5\mu\text{m}} \sim 4.5\mu\text{m}/\lambda_{\text{H}\alpha} - 1 \sim 6$ .) The strong  $\text{H}\alpha$  emission line influences the  $K$ -correction so as to increase the number of detectable SNe at  $z_{\text{H}\alpha, 4.5\mu\text{m}}$ . This reduces the apparent drop in the SFR, if the reionization feature occurs at redshifts just above  $z_{\text{H}\alpha, 4.5\mu\text{m}}$  (and, likewise, increases the size of the drop if the reionization feature occurs just below  $z_{\text{H}\alpha, 4.5\mu\text{m}}$ ). The detectability of the reionization feature is only affected at  $z_{\text{H}\alpha, 4.5\mu\text{m}} \sim 6$  due to the combination of (i) and (ii) above. The presence of the  $\text{H}\alpha$  line is nevertheless potentially important, because reionization could have occurred around this redshift (Mesinger & Haiman 2004). This highlights the need for an improved statistical description of SNe template spectra from low-redshift data, allowing one to “model out” an offending emission line, or for observations of the high- $z$  SNe in a different filter (as can be seen from Figure 5, using the 3.5  $\mu\text{m}$  filter bypasses this issue).

In order to obtain high-redshift SNRs, several simplifications have been made in our analysis, involving the poorly constrained redshift evolution (more precisely, the lack of evolution) of the stellar initial mass function (IMF), SN progenitors, star formation efficiency, SN lightcurves and spectra, etc. Because of this, the numbers presented in Figures 4 and 5 should be regarded only as rough estimates of what a future survey might achieve. However, our main conclusions rely on a sudden feature in the redshift evolution of the SNR, and should remain valid, as long as evolution in other parameters occurs over a much wider redshift range than the reionization feature (Wyithe & Loeb 2004a; Barkana & Loeb 2004b), and as long as the pre-reionization SNR is not significantly reduced (since the latter would diminish the confidence at which any subsequent drop in the SNR, caused by reionization, could be detected).

### 3.2.1. Pop-III SNe

As discussed above, high-redshift SNe whose progenitor stars are formed from metal-free gas within minihalos could be intrinsically very different from the low-redshift SNe, due to differences in the progenitor environments (e.g. very low metallicities; Abel et al. 2002; Bromm et al. 2002). If such differences could be identified and detected, then these “pop-III” SNe could provide valuable information about primordial stars

and their environments. Indeed, Wise & Abel (2005) recently studied the redshift–distribution of such primordial SNe, but only briefly addressed the issue of their detectability. In order to directly assess the number of such SNe among the hypothetical SNe samples we obtained here, in Figure 6, we plot the fraction of SNe whose progenitor stars are located in minihalos. The solid curve assumes our fiducial model with a Salpeter IMF and  $\epsilon_{*minihalo} = 0.1$ ; the dotted curve assumes that each minihalo produces only a single star, and hence a single SN, over a dynamical time (assuming that strong feedback from this star disrupts any future star formation; as in Wise & Abel 2005). The figure shows that with an unevolving star formation efficiency, progenitor stars in minihalos would account for over half of the SNe at  $z \gtrsim 9$ . On the other hand, in the extreme case of a single SNe per minihalo, progenitor stars in minihalos would account for less than  $\sim 1\%$  of the  $z \sim 10$  SNe (although at the earliest epochs,  $z \gtrsim 22$ , they would still constitute over half of all SNe). Given the overall detection rate of several hundred  $z \gtrsim 10$  SNe with a 1 year *JWST* survey we have found above, even in this extreme case, Figure 6 implies that several of these SNe could be caused by pop–III stars.

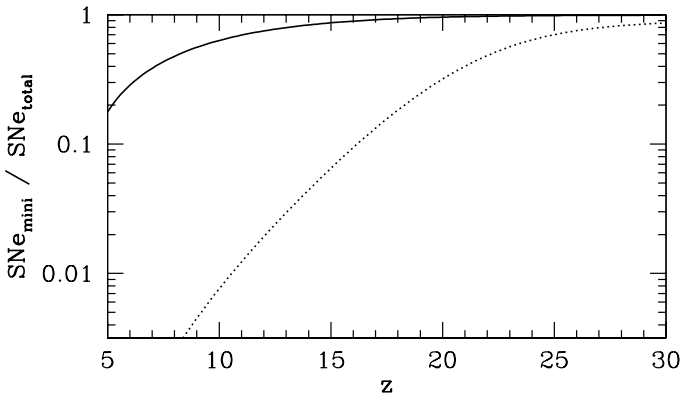


FIG. 6.— Fraction of SNe whose progenitor stars are located in minihalos. The solid curve assumes our fiducial model with a Salpeter IMF and  $\epsilon_{*minihalo} = 0.1$ ; the dotted curve assumes that each minihalo produces only a single star (and therefore a single SN) over a dynamical time.

### 3.2.2. Varying Minihalo Star–Formation Efficiency

The uncertainties in the typical star–formation efficiency in minihalos can also directly influence our estimates for the detectability of the reionization feature. We have already shown that the feature is detectable from SNe distributions even in the absence of star formation in minihalos, but only provided that halos do not self-shield effectively and the virial temperature for star–formation is raised well above  $10^4\text{K}$  (e.g. see the right panels of figures 4b and 5b). If self-shielding is very effective, the reionization drop is determined by the evolution of the SFR in minihalos. In Figure 7, we plot the S/N with which the reionization feature is detectable from a fiducial one–year survey, as a function of the assumed (constant) star–formation efficiency in minihalos,  $\epsilon_{*minihalo}$ . The three curves correspond to  $z_{re} = 7$  (solid curve), 10 (dotted curve), 13 (dashed curve). All curves assume the transition  $T_{vir}(z > z_{re}) \gtrsim 300\text{K} \rightarrow T_{vir}(z < z_{re}) \gtrsim 10^4\text{K}$ , as well as a flux density threshold of  $3\text{ nJy}$  ( $t_{exp} = 10^5\text{s}$  with the  $4.5\text{ }\mu\text{m}$  *JWST* filter), and no dust extinction. The figure shows that in this case, the reionization signal is detectable at  $6 \lesssim z_{re} \lesssim 13$  with  $S/N > 2$  as long as the star formation efficiency in minihalos exceeds  $\epsilon_{*minihalo} \sim 0.05$ .

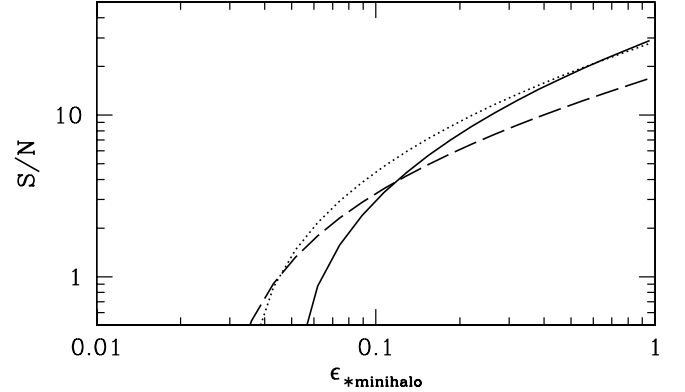


FIG. 7.— S/N with which reionization can be detected as a function of the assumed (constant) star–formation efficiency in minihalos,  $\epsilon_{*minihalo}$ . The three curves correspond to three different reionization redshifts  $z_{re} = 7$  (solid curve), 10 (dotted curve), and 13 (dashed curve). All curves assume the transition  $T_{vir}(z > z_{re}) \gtrsim 300\text{K} \rightarrow T_{vir}(z < z_{re}) \gtrsim 10^4\text{K}$ , as well as a flux density threshold of  $3\text{ nJy}$  ( $t_{exp} = 10^5\text{s}$  with the  $4.5\text{ }\mu\text{m}$  *JWST* filter), no dust extinction, and a  $t_{surv} = 1\text{yr}$  survey (or, correspondingly, using  $1\text{yr}/(2t_{exp})$  images with a  $2.3' \times 4.6'$  FOV).

### 3.2.3. Varying $\Delta z_{re}$

As mentioned previously, the width of a reionization feature, which we have parameterized by  $\Delta z_{re}$  (see the clarification below eq.(6)), is uncertain. In our fiducial model we have assumed to study fairly sharp features with  $\Delta z_{re} = 1$ . Here we investigate the detectability of more extended reionization features. In Figure 8, we plot the maximum reionization redshift,  $z_{re\text{ max}}$ , up to which the reionization signal would be detectable at  $S/N \gtrsim 3$  in a 1 yr survey, as a function of  $\Delta z_{re}$ . To approximate the redshift–smearing due to any self-regulation or scatter, we simply follow the procedure discussed above (following eq.6), but take averages of the SNR in increasingly wider redshift bins prior to and following  $z_{re}$ . This effectively averages the SNR in two bins whose mean redshifts are separated by  $\Delta z_{re}$  and mimics a suppression that is spread-out over this redshift, rather than instantaneous. A reionization feature occurring in the range  $6 \lesssim z_{re} \lesssim z_{re\text{ max}}$ , smeared over a redshift range of  $\Delta z_{re}$ , would be detectable out to the redshifts shown in

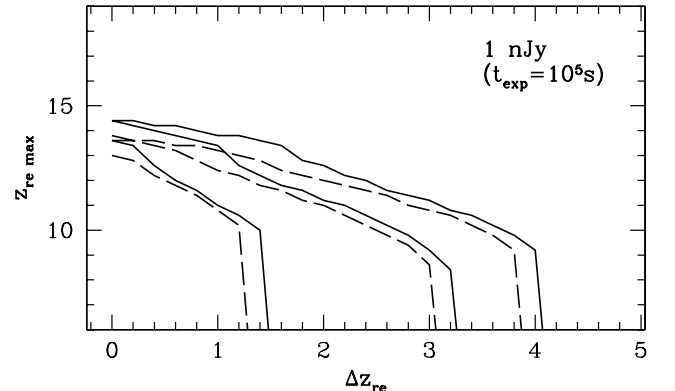


FIG. 8.— Maximum reionization redshift,  $z_{re\text{ max}}$ , up to which the reionization signal would be detectable at  $S/N \gtrsim 3$  in a 1 yr survey, as a function of  $\Delta z_{re}$ . The curves correspond to the reionization transitions of  $T_{vir} \gtrsim 300\text{K} \rightarrow 10^4\text{K}$ ,  $T_{vir} \gtrsim 300\text{K} \rightarrow 4.5 \times 10^4\text{K}$ , and  $T_{vir} \gtrsim 300\text{K} \rightarrow 1.1 \times 10^5\text{K}$ , (left to right). Solid curves correspond to no dust obscuration; dashed curves include dust. All curves assume a detection threshold of  $1\text{ nJy}$ , analogous to  $t_{exp} = 10^5\text{s}$  exposures in the  $3.5\text{ }\mu\text{m}$  *JWST* band.

Figure 8. The curves correspond to the reionization transitions of  $T_{\text{vir}} \gtrsim 300 \text{ K} \rightarrow 10^4 \text{ K}$ ,  $T_{\text{vir}} \gtrsim 300 \text{ K} \rightarrow 4.5 \times 10^4 \text{ K}$ , and  $T_{\text{vir}} \gtrsim 300 \text{ K} \rightarrow 1.1 \times 10^5 \text{ K}$ , (left to right). Solid curves correspond to no dust obscuration; dashed curves include dust. All curves assume a detection threshold of 1 nJy, analogous to  $t_{\text{exp}} = 10^5 \text{ s}$  exposures in the  $3.5 \mu\text{m}$  *JWST* band. From the figure, one can note that the most optimistic scenario ( $T_{\text{vir}} \gtrsim 300 \text{ K} \rightarrow 1.1 \times 10^5 \text{ K}$ ), a reionization feature is detectable even if it occurs over a redshift range  $\Delta z_{\text{re}} \sim 4$ . In other cases, the detection of the reionization feature requires  $\Delta z_{\text{re}} \lesssim 1 - 3$ .

### 3.2.4. Feasibility of a Fairly Sudden Drop in SNe Rates

The details and duration of the reionization epoch, and hence the shape and width of the drop in SNe rates, are unknown at this time. Results from *WMAP* and the SDSS QSOs offer suggestive, albeit not conclusive, evidence that reionization was extended in redshift.<sup>4</sup> If reionization is indeed quite extended in redshift ( $\Delta z \sim 10$ ), the associated drop in the SFR and SNR could be smeared out too much to be detectable. However, even in the pessimistic (as it pertains to our analysis below) scenario where some effective *width* of the reionization feature is as large as  $\Delta z \sim 10$ , the *shape* of the feature need not be smooth, and could contain “sharp” ( $\Delta z_{\text{re}} \sim 1$ ) drops. Such transitions are probable in reionization histories in which different sources dominate different epochs (e.g. Haiman & Holder 2003).

The relevant process in determining the width and shape of the drop in SNRs is the evolution of the volume filling factor of ionized regions and their correlation with the small, vulnerable halos<sup>5</sup> whose SFRs are sensitive to the thermal state of the IGM. In other words, the sharpness of the drop in SNRs, in each epoch during reionization, will depend on:

1. the nature of the dominant ionizing sources
2. the ionizing efficiency of the dominant ionizing sources
3. the level of synchronization of small halo formation with the formation of dominant ionizing sources
4. the level of synchronization of the dominant ionizing sources

If the small, vulnerable halos themselves are the dominant ionizing sources at that particular epoch, then a sharp reionization feature could result if: (2) is high, and (3) is moderate (in this case (3) and (4) are the same). If (3) is too high (i.e. the formation of small, vulnerable halos is very clustered in time and space), then negative feedback from the ionizing radiation could delay substantial growth of HII bubbles until small halos are no longer forming prodigiously enough to serve as signposts for reionization. If (3) is too low, there might not be enough affected halos to notice the suppression; or large, isolated patches might have to wait a long time for their own ionizing sources to form (if (2) is not very high), thus smearing out the signal through pure cosmic variance.

<sup>4</sup>Note that there are two, often confused processes and time-scales associated with reionization: (i) the increase in intensity of the ionizing background and the mean free path of ionizing photons and (ii) the increase in the filling factor of ionized regions. For the purposes of this paper, we concern ourselves with (ii).

<sup>5</sup>Note the distinction here between “small halos” and “minihalos”. In the discussion below, we use the term small halos to denote all halos whose SFRs will be suppressed by reionization. Thus small halos include minihalos as well as larger halos, depending on their susceptibility to negative photo-heating feedback.

If the small, vulnerable halos are not the dominant ionizing sources (as would be expected for the later periods of an extended reionization), then a sharp feature could result if (2) is high enough to reasonably counter cosmic variance. However, we could relax our fine-tuning on (3) above, since feedback no longer hinders the growth of HII regions. There merely need to be enough small halos at that epoch to act as signposts for reionization. From Figure 6, we see that this a reasonable assumption, especially given the fact that most small halos which are still forming at such late stages are probably not going to be very near the large overdensities which were likely to be ionized during earlier stages (Furlanetto & Oh 2005; Ricotti et al. 2002). We also require (4) to be reasonably high (i.e. that the dominant ionizing sources appear around the same time, without too much cosmic scatter). Below, we further quantify such a scenario.

One can get a sense of the possible shapes of the reionization feature through an estimate of the evolution of the filling factor of ionized regions,  $F_{\text{HII}}(z)$ , (c.f. Barkana & Loeb 2001; Haiman & Holder 2003):

$$\frac{dF_{\text{HII}}(z)}{dt} = \epsilon_* f_{\text{esc}} \frac{N_{\text{ph/b}}}{0.76} \frac{dF_{\text{col}}(> M_{\text{min}}(z), z)}{dt} - \alpha_B C \langle n_{\text{H}}^0 \rangle (1+z)^3 F_{\text{HII}}. \quad (7)$$

Here  $f_{\text{esc}}$  is the escape fraction of ionizing photons,  $N_{\text{ph/b}}$  is the number of ionizing photons per baryon emitted by a typical source,  $F_{\text{col}}(> M, z)$  is the fraction of baryons that reside in collapsed halos with a total mass greater than  $M$  at redshift  $z$ ,  $\alpha_B$  is the hydrogen case B recombination coefficient,  $C \equiv \langle n_{\text{H}}^2 \rangle / \langle n_{\text{H}} \rangle^2$  is the clumping factor, and  $\langle n_{\text{H}}^0 \rangle$  is the current hydrogen number density. The first term on the right hand side accounts for “new” ionizations contributing to the growth of the HII regions and the last term on the right hand side accounts for “old” reionizations due to recombinations inside the HII region. This equation is a very rough approximation, as it does not include feedback effects, light travel time, and it does not accurately model the period when bubbles start overlapping (i.e.  $F_{\text{HII}}(z) \sim 1$ ). However, it can suffice for the crude estimates we are making here.

In Figure 9, we plot  $F_{\text{HII}}(z)$  for several values of  $M_{\text{min}}(z)$  corresponding to redshift-independent values of  $T_{\text{vir}} = 300 \text{ K}$ ,  $10^4 \text{ K}$ , and  $10^5 \text{ K}$ , from right to left in the figure. The plot assumes values of  $(\epsilon_*, f_{\text{esc}}, N_{\text{ph/b}}, C) = (0.1, 0.1, 4000, 4)$ . From the figure, it is evident that fairly rapid growth of  $F_{\text{HII}}(z)$  is possible for  $F_{\text{HII}}(z) \gtrsim 0.1$ . For example, the  $T_{\text{vir}} \gtrsim 10^5 \text{ K}$  curve goes from  $F_{\text{HII}} \sim 0.3$  to  $F_{\text{HII}} \sim 0.8$  in the redshift interval  $z \sim 8.5 \rightarrow 7$ . So SNe in roughly 50% of small halos could be wiped out in a redshift interval of only  $\Delta z_{\text{re}} \sim 1.5$ . Comparing with Figures 4a, 5a or 6, one can see that this could result in a fairly large, easily detectable drop in the SNRs.

To summarize, we outline a likely reionization scenario. An early reionization epoch could be driven by minihalos. Feedback processes can stall reionization at a constant or even decreasing filling factor of ionized regions. Then a later population of more massive halos ( $T_{\text{vir}} \sim 10^4 - 10^5 \text{ K}$ ) could complete the ionization process on time-scales corresponding to  $\Delta z_{\text{re}} \sim 1 - 2$ . The research we present here suggests that this later epoch is detectable through an accompanying drop in the SNRs.

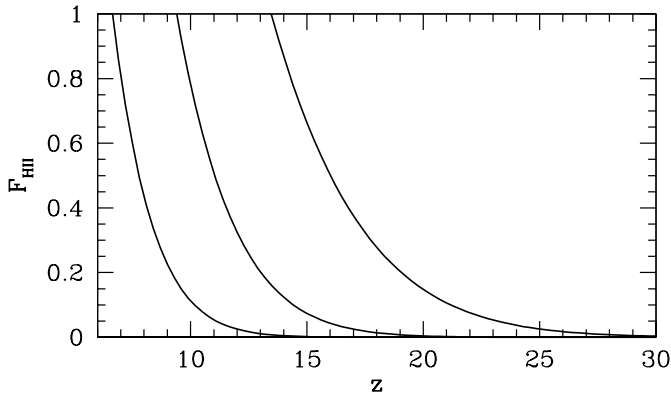


FIG. 9.— Simple models of the evolution of the filling factor of ionized regions,  $F_{\text{HII}}(z)$ , for several values of  $M_{\text{min}}(z)$  corresponding to redshift-independent values of  $T_{\text{vir}} = 300 \text{ K}$ ,  $10^4 \text{ K}$ , and  $10^5 \text{ K}$ , right to left.

#### 4. CONCLUSIONS

We obtain detailed, high-redshift SNe rates which could be detected in future infrared surveys, such as *JWST*. Our method uses the extended Press-Schechter formalism to generate high-redshift SFRs and SNRs. We empirically calibrate our model using the observed properties of local SNe, such as their lightcurves, fiducial spectra, as well as dust corrected and uncorrected peak magnitude distributions, to predict the detectable high- $z$  SNRs.

During reionization, the ionizing background radiation heats the IGM and could dramatically suppress gas accretion and star formation in low-mass halos. As a result, reionization may be accompanied by a drop in the SFR and the corresponding SNR. The size of the drop is uncertain, since the ability of the gas in low-mass halos to cool and self-shield against the ionizing radiation is poorly constrained at high redshifts. However, we argued, using specific illustrative models, that a relatively sharp feature is feasible. Using the SNRs we generate, we then analyze the prospects of detecting such a feature with future SNe observations, specifically those obtainable with *JWST*.

We find that 4 – 24 SNe may be detectable from  $z \gtrsim 5$  at the sensitivity of 3 nJy (requiring  $10^5 \text{ s}$  exposures in a  $4.5 \mu\text{m}$  band) in each  $\sim 10 \text{ arcmin}^2$  *JWST* field. In a hypothetical one year survey, we expect to detect up to thousands of SNe per unit redshift at  $z \sim 6$ . Our results imply that, for most scenarios, high-redshift SNe observations can be used to detect fairly sharp features in the reionization history (occurring over  $\Delta z_{\text{re}} \sim 1 - 3$ ) out to  $z \sim 13$ , as well as set constraints on the photo-ionization heating feedback on low-mass halos at the reionization epoch. Specifically, for a wide range of scenarios at  $z_{\text{re}} \lesssim 13$ , the drop in the SNR due to reionization can be detected at  $S/N \gtrsim 3$  with only tens of deep *JWST* exposures. Our results therefore suggest that future searches for high- $z$  SNe could be a valuable new tool, complementing other techniques, to study the process of reionization, as well as the feedback mechanism that regulates it.

We thank Rosalba Perna, David Helfand, Avi Loeb, Tom Abel, Rennan Barkana, Peng Oh, and Steven Furlanetto for useful discussions. ZH gratefully acknowledges support by the NSF through grants AST-0307200 and AST-0307291, and by NASA through grants NNG04GI88G and NNG05GF14G.

- Abel, T., Bryan, G. L., & Norman, M. L. 2002, *Science*, 295, 93  
 Adelberger, K. L., & Steidel, C. C. 2000, *ApJ*, 544, 218  
 Barkana, R., & Loeb, A. 2000, *ApJ*, 539, 20  
 —. 2001, *Phys. Rep.*, 349, 125  
 —. 2004a, *ApJ*, 601, 64  
 —. 2004b, *ApJ*, 609, 474  
 Baron, E. et al. 2000, *ApJ*, 545, 444  
 Bromm, V., Coppi, P. S., & Larson, R. B. 2002, *ApJ*, 564, 23  
 Bromm, V., Ferrara, A., Coppi, P. S., & Larson, R. B. 2001, *MNRAS*, 328, 969  
 Bromm, V., & Loeb, A. 2002, *ApJ*, 575, 111  
 Bryan, G. L., & Norman, M. L. 1998, *ApJ*, 495, 80  
 Bunker, A. J., Stanway, E. R., Ellis, R. S., & McMahon, R. G. 2004, *MNRAS*, 355, 374  
 Cappellaro, E., Turatto, M., Tsvetkov, D. Y., Bartunov, O. S., Pollas, C., Evans, R., & Hamuy, M. 1997, *A&A*, 322, 431  
 Cen, R. 2003, *ApJ*, 591, L5  
 Cen, R., & McDonald, P. 2002, *ApJ*, 570, 457  
 Cen, R., & Ostriker, J. P. 1992, *ApJ*, 399, L113  
 Choudhury, T. R., & Srianand, R. 2002, *MNRAS*, 336, L27  
 Dahlén, T., & Fransson, C. 1999, *A&A*, 350, 349  
 Dijkstra, M., Haiman, Z., Rees, M. J., & Weinberg, D. H. 2004, *ApJ*, 601, 666  
 Doggett, J. B., & Branch, D. 1985, *ApJ*, 90, 2303  
 Efstathiou, G. 1992, *MNRAS*, 256, 43P  
 Fan, X. et al. 2004, *AJ*, 128, 515  
 Furlanetto, S. R., & Oh, S. P. 2005, astro-ph/0505065  
 Gabasch, A. et al. 2004, *ApJ*, 616, L83  
 Giavalisco, M. et al. 2004, *ApJ*, 600, L103  
 Gnedin, N. Y. 1996, *ApJ*, 456, 1  
 —. 2000, *ApJ*, 542, 535  
 Haiman, Z., Abel, T., & Rees, M. J. 2000, *ApJ*, 534, 11  
 Haiman, Z., & Holder, G. P. 2003, *ApJ*, 595, 1  
 Haiman, Z., & Loeb, A. 1999, *ApJ*, 519, 479  
 Hamuy, M. et al. 2001, *ApJ*, 558, 615  
 Heger, A., Fryer, C. L., Woosley, S. E., Langer, N., & Hartmann, D. H. 2003, *ApJ*, 591, 288  
 Holder, G., Haiman, Z., & Mohr, J. J. 2001, *ApJ*, 560, L111  
 Kitayama, T., & Ikeuchi, S. 2000, *ApJ*, 529, 615  
 Kogut, A. et al. 2003, *ApJS*, 148, 161  
 Lacey, C., & Cole, S. 1993, *MNRAS*, 262, 627  
 Leibundgut, B., & Suntzeff, N. B. 2003, *LNP Vol. 598: Supernovae and Gamma-Ray Bursters*, 598, 77  
 Lilly, S. J., Le Fevre, O., Hammer, F., & Crampton, D. 1996, *ApJ*, 460, L11+  
 Madau, P., della Valle, M., & Panagia, N. 1998, *MNRAS*, 297, L17+  
 Madau, P., Ferguson, H. C., Dickinson, M. E., Giavalisco, M., Steidel, C. C., & Fruchter, A. 1996, *MNRAS*, 283, 1388  
 Madau, P., Meiksin, A., & Rees, M. J. 1997, *ApJ*, 475, 429  
 Mesinger, A., & Haiman, Z. 2004, *ApJ*, 611, L69  
 Mesinger, A., Haiman, Z., & Cen, R. 2004, *ApJ*, 613, 23  
 Mesinger, A., Perna, R., & Haiman, Z. 2005, *ApJ*, 623, 1  
 Miralda-Escude, J., & Rees, M. J. 1997, *ApJ*, 478, L57+  
 Nemiroff, R. J. 2003, *AJ*, 125, 2740  
 Patat, F., Barbon, R., Cappellaro, E., & Turatto, M. 1994, *A&A*, 282, 731  
 Richardson, D., Branch, D., Casebeer, D., Millard, J., Thomas, R. C., & Baron, E. 2002, *AJ*, 123, 745  
 Ricotti, M., Gnedin, N. Y., & Shull, J. M. 2002, *ApJ*, 575, 49  
 Shapiro, P. R., Giroux, M. L., & Babul, A. 1994, *ApJ*, 427, 25  
 Shapiro, P. R., Iliev, I. T., & Raga, A. C. 2004, *MNRAS*, 348, 753  
 Sokasian, A., Yoshida, N., Abel, T., Hernquist, L., & Springel, V. 2004, *MNRAS*, 350, 47  
 Somerville, R. S., Primack, J. R., & Faber, S. M. 2001, *MNRAS*, 320, 504  
 Spergel, D. N. et al. 2003, *ApJS*, 148, 175  
 Strolger, L. et al. 2004, *ApJ*, 613, 200  
 Thoul, A. A., & Weinberg, D. H. 1996, *ApJ*, 465, 608  
 Wang, Y. et al. 2004, *American Astronomical Society Meeting Abstracts*, 205,  
 Wise, J. H., & Abel, T. 2005, *ApJ*, submitted, astro-ph/0411558  
 Wyithe, J. S. B., & Loeb, A. 2004a, *Nature*, 432, 194  
 —. 2004b, *Nature*, 427, 815